

2-2020

High-field spatial imaging of charge transport in silicon at low temperature

C. Stanford

R. A. Moffatt

N. A. Kurinsky

P. L. Brink

Blas Cabrera

See next page for additional authors

Follow this and additional works at: <https://scholarcommons.scu.edu/physics>



Part of the [Physics Commons](#)

Recommended Citation

Stanford, C., Moffatt, R. A., Kurinsky, N. A., Brink, P. L., Cabrera, B., Cherry, M., Insulla, F., Kelsey, M., Ponce, F., Sundqvist, K., Yellin, S., & Young, B. A. (2020). High-field spatial imaging of charge transport in silicon at low temperature. *AIP Advances*, 10(2), 025316. <https://doi.org/10.1063/1.5131171>

© 2020 Author(s). All article content, except where otherwise noted, is licensed under a Creative Commons Attribution (CC BY) license (<http://creativecommons.org/licenses/by/4.0/>).

This Article is brought to you for free and open access by the College of Arts & Sciences at Scholar Commons. It has been accepted for inclusion in Physics by an authorized administrator of Scholar Commons. For more information, please contact rscroggin@scu.edu.

Authors

C. Stanford, R. A. Moffatt, N. A. Kurinsky, P. L. Brink, Blas Cabrera, Matthew Cherry, F. Insulla, M. Kelsey, F. Ponce, K. Sundqvist, S. Yellin, and Betty A. Young

RESEARCH ARTICLE | FEBRUARY 11 2020

High-field spatial imaging of charge transport in silicon at low temperature

C. Stanford ; R. A. Moffatt; N. A. Kurinsky ; P. L. Brink; B. Cabrera ; M. Cherry; F. Insulla; M. Kelsey; F. Ponce ; K. Sundqvist; S. Yellin ; B. A. Young



AIP Advances 10, 025316 (2020)

<https://doi.org/10.1063/1.5131171>

 CHORUS



Articles You May Be Interested In

Enrichment of the Intra-Cluster Medium Due to AGN Outflows Induced by Late-Type Galaxies

AIP Conference Proceedings (December 2009)

Dark Matter, AGNs and Relativistic Jets

AIP Conference Proceedings (May 2003)

The Big Picture of AGN Feedback: Black Hole Accretion and Galaxy Evolution in Multiwavelength Surveys

AIP Conference Proceedings (December 2009)

12 November 2024 17:34:48

AIP Advances

Why Publish With Us?



19 DAYS
average time
to 1st decision



500+ VIEWS
per article (average)



INCLUSIVE
scope

[Learn More](#)



High-field spatial imaging of charge transport in silicon at low temperature

Cite as: AIP Advances 10, 025316 (2020); doi: 10.1063/1.5131171

Submitted: 9 October 2019 • Accepted: 26 January 2020 •

Published Online: 11 February 2020



View Online



Export Citation



CrossMark

C. Stanford,^{1,a)} R. A. Moffatt,¹ N. A. Kurinsky,^{2,3} P. L. Brink,⁴ B. Cabrera,^{1,4,b)} M. Cherry,⁴ F. Insulla,¹ M. Kelsey,⁴ F. Ponce,¹ K. Sundqvist,⁵ S. Yellin,¹ and B. A. Young⁶

AFFILIATIONS

¹Department of Physics, Stanford University, Stanford, California 94305, USA

²Fermi National Accelerator Laboratory, Center for Particle Astrophysics, Batavia, Illinois 60510, USA

³Kavli Institute for Cosmological Physics, University of Chicago, Chicago, Illinois 60637, USA

⁴SLAC National Accelerator Laboratory/Kavli Institute for Particle Astrophysics and Cosmology, 2575 Sand Hill Road, Menlo Park, California 94025, USA

⁵Department of Physics, San Diego State University, San Diego, California 92182, USA

⁶Department of Physics, Santa Clara University, Santa Clara, California 95053, USA

^{a)} Author to whom correspondence should be addressed: cstan4d@stanford.edu

^{b)} Electronic mail: cabrera@stanford.edu

ABSTRACT

We present direct imaging measurements of charge transport across a 1 cm × 1 cm × 4 mm-thick crystal of high purity silicon (~15 kΩ-cm) at temperatures of 5 K and 500 mK. We use these data to measure lateral diffusion of electrons and holes as a function of the electric field applied along the [111] crystal axis and to verify our low-temperature Monte Carlo software. The range of field strengths in this paper exceed those used in our previous study [R. A. Moffatt *et al.*, Appl. Phys. Lett. **114**, 032104 (2019)] by a factor of 10 and now encompass the region in which some recent silicon dark matter detectors operate [R. Agnese *et al.*, Phys. Rev. Lett. **121**, 051301 (2018)]. We also report on a phenomenon of surface charge trapping, which can reduce expected charge collection.

© 2020 Author(s). All article content, except where otherwise noted, is licensed under a Creative Commons Attribution (CC BY) license (<http://creativecommons.org/licenses/by/4.0/>). <https://doi.org/10.1063/1.5131171>

Recent advances in silicon (Si) detector technology have enabled a single-charge resolving readout of cryogenic crystals [SuperCDMS High Voltage eV-scale (HVeV)]^{1–3} and skipper CCDs.^{4,5} In particular, HVeV detectors attain single-charge resolution via the phonon-assisted Neganov–Trofimov–Luke amplification^{6,7} in which a voltage is applied across the crystal to produce phonons by accelerating charge carriers. The resulting signal is, thus, highly dependent on the details of charge–phonon interactions. In an earlier work,⁸ we studied the charge–phonon dynamics in Si at small drift fields, comparable to those employed in monolithic charge detectors.

To better understand the spatial distributions of charge carriers at the very large electric fields utilized by SuperCDMS HVeV detectors,² these measurements need to be extended to higher field strengths. In addition, we need to demonstrate the impact of charge

buildup, electric field, and temperature on the final positions of electrons and holes excited by laser pulses in a high-purity silicon crystal, and compare these results to expectations from simulations, in order to ensure proper event reconstruction in these detectors.

Si is an indirect bandgap semiconductor with electron energy minima (valleys) that are displaced from zero in momentum space along the {100} crystal axes. At room temperature, electrons are energetically able to tunnel between these valleys, and thus charge propagation is approximately anisotropic, but near 0 K electrons become isolated in these valleys producing highly anisotropic electron collection patterns. Figure 1 (left) shows the Brillouin zone for (111) Si, including the surfaces of constant energy about these minima. They appear oval in shape because the surfaces of equal energy are themselves highly anisotropic; electrons have effective masses of

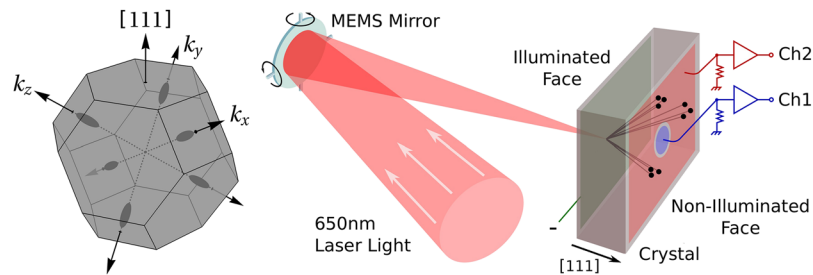


FIG. 1. Left: the first Brillouin zone for (111) Si. The electron energy minima, or valleys, are located near the edge of the zone in the k_x , k_y , and k_z directions (black ovals). At low fields, electrons propagate along the valley axes and produce three distinct charge populations. Right: the detector, which consists of a $1\text{ cm} \times 1\text{ cm} \times 4\text{ mm}$ crystal of high purity silicon, and the laser mechanism, which uses a MEMS mirror to scan a focused beam of light pulses across the back face of the crystal in order to produce a 2D image. The crystal is biased via a parquet electrode on the illuminated face. The non-illuminated face features unbiased inner (blue) and outer (red) electrodes for charge collection. Reproduced with permission from Moffatt *et al.*, Appl. Phys. Lett. **114**, 032104 (2019). Copyright 2019 AIP Publishing LLC.

$0.98 m_e$ and $0.19 m_e$ in the momentum space directions parallel and perpendicular to the valley axis, respectively.⁹

If a small electric field is applied to the crystal along the [111] direction, free electrons will tend to remain aligned with their individual valley axis rather than the applied field. Three distinct charge populations will then propagate through the crystal and reach the surface. As the electric field is increased, each drifting electron carries more energy. Energetic electrons are capable of emitting an optical phonon and transitioning between Brillouin zone minima;^{9–12} this is called an intervalley scattering event. At higher field strengths, this scattering becomes so frequent that the electrons effectively propagate in the mean valley direction, in this case along [111] (which we label the z -direction). At the same time, the propagating electrons move with an xy -diffusion consistent with a 2D random walk. We directly imaged this phenomenon in our previous paper⁸ up to field strengths of 50 V cm^{-1} .

In contrast, holes in Si have their energy band minima at $k = 0$ in momentum space and therefore propagate along the applied field even at low strengths. The resulting spatial distribution of charges arriving at the Si surface is still not perfectly Gaussian, however, because of the inherently anisotropic dispersion relation for holes, as detailed in other papers^{13–15} and first imaged by Moffatt *et al.*⁸

In this paper, we present a direct measurement of the xy -diffusion of electrons and holes in (111) Si under electric field strengths up to 500 V cm^{-1} , a factor of 10 increase over our previous paper.⁸ With these field strengths, we are able to achieve the same conditions as those used with our HVeV dark matter detectors,² so the diffusion measurements made here will allow us to refine the charge transport models used in the SuperCDMS detector Monte Carlo. In particular, we find that when an ionization site occurs near the crystal's side wall, the xy -diffusion can result in some of the charges hitting the wall and stopping before reaching the charge collection electrodes. Such fractional charge collection events are a significant background in the HVeV detectors,² so in order to perform a background subtraction, it is critical to have a proper model of the xy -diffusion in these devices.

This paper also reports on the phenomenon of charge buildup on the surface of Si crystals, as it was discovered to be a relevant factor when modeling the diffusion of both electrons and holes.

We observed that as propagating charges approached a cluster of like-charges trapped near the (111) surface electrodes, their paths were deflected outward (away from the z -direction), resulting in greater xy diffusion than expected.

A schematic of the detector and the accompanying laser system used for this measurement is shown in Fig. 1 (right). The crystal was cut from a 4 mm-thick wafer of undoped ultra-high-purity float-zone silicon ($\sim 15\text{ k}\Omega\text{-cm}$). The residual impurity was measured to be p-type with a concentration of 10^{12} cm^{-3} . The front (illuminated) and back (non-illuminated) faces of the crystal are $1\text{ cm} \times 1\text{ cm}$ and lie in the (111) plane. The front face is patterned with an aluminum-tungsten mesh electrode with 20% coverage.¹⁶ The back face features a small, inner electrode in the center of the face, circular in shape with a diameter of $160\text{ }\mu\text{m}$, separated by a $10\text{ }\mu\text{m}$ gap from the outer electrode, which covers the rest of the face. These electrodes are separately contacted but are held at the same voltage to provide a near-uniform field throughout the crystalline substrate.

Free electrons and holes are produced at the front face of the crystal by exposing it to pulses of 650 nm laser light, focused to a single spot on the face. An exposure is typically a “pulse train” of twenty $200\text{ }\mu\text{W}$, 50 ns pulses, with a 1 ms delay between each pulse. This intensity was set by trial and error to be above the noise floor of the detector, while at the same time not saturating the electronics. The wavelength of 650 nm corresponds to a photon energy of 1.9 eV, which is above the silicon bandgap, and therefore produces electron-hole pairs in the crystal. Either the electrons or holes (depending on the sign of the bias voltage) freed by a light pulse will quickly propagate through the crystal and produce a voltage pulse in the electrodes on the back face of the detector. The pulses pass through a cryogenic amplifier circuit based on Sony 3SK165 MESFETs, described in detail by Moffatt,¹⁷ and are recorded using a National Instruments USB-6009 and an Agilent DWO6104A oscilloscope. The data acquisition system records a 20 ms trace for both the inner and outer electrodes [see Fig. 2 (top)]. In post-processing, the 20 pulses contained in each 20 ms trace are averaged to obtain a single value for the pulse amplitude for each electrode.

In order to reduce scattering of propagating charges by background phonons, the crystal is cooled in a ^3He cryostat with the capability of reaching temperatures down to 500 mK.

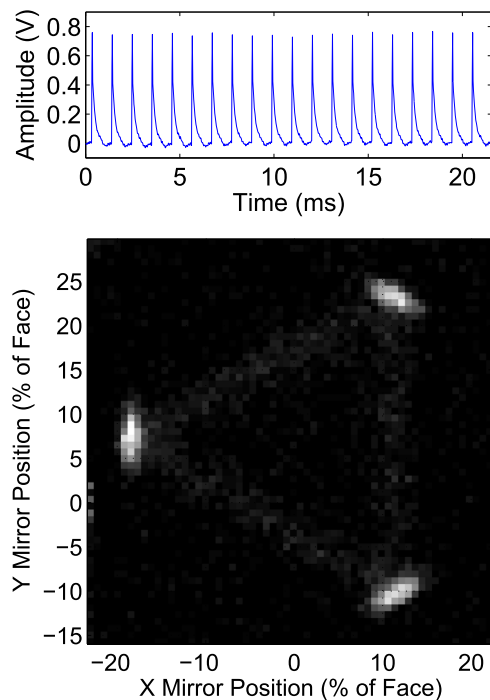


FIG. 2. Top: the time-dependent electrical response of the inner electrode resulting from a train of 20 laser pulses, corresponding to position (12,23) in the bottom figure. Bottom: a 2D image of the charge pattern at a low field (-10 V cm^{-1}) with the white spots indicating the regions where more charge was collected.

The position of the laser's focal point on the front face of the detector is controlled by a Micro-Electromechanical Systems (MEMS) mirror.¹⁸ The full width at half maximum of the spot was measured to be approximately $60 \mu\text{m}$, as was determined by scanning the focal point of the laser over a small aluminum feature of known size on the front face of the crystal and measuring the impact.

During each imaging measurement, the mirror is moved in such a way as to make the laser perform a raster scan across the front

face of the crystal, pausing briefly at each position to enable periodic neutralization of the trapping sites in the crystal. The precise neutralization procedure involves electrically grounding both faces of the detector while illuminating the crystal with diffuse 650 nm light for 1 s, before reapplying the voltage bias. Without performing this step, the signals get smaller with time, implying that the drifting charges are being captured in trapping sites. Periodic neutralization limits this effect.

At every point in the raster scan, the small inner electrode is sampling a different part of the charge pattern that arrives at the back face. Therefore, by plotting the average amplitude of the inner electrode as a function of laser spot position, we obtain a 2D image of the charge pattern. Figure 2 (bottom) is an example of an image taken at a low field (-10 V cm^{-1}) with the white spots indicating the regions where more charge was collected.

The first measurements made in this new study yielded full 2D charge pattern images for both electrons and holes over a range of field strengths from 10 V cm^{-1} to 500 V cm^{-1} . To visualize the changing pattern as a function of voltage, we reduced the images to their 50% contours and overlaid them, as shown in Fig. 3.

Figure 3 (left) shows that at -10 V/cm (blue), the electrons largely remain in their original valleys and thus produce the expected “tri-lobe” shape. At -20 V/cm (orange), the electron mean free path between intervalley scatters is on the order of the crystal's 4 mm thickness. Electrons scatter only once and will end up somewhere between the three lobes, which leads to a line appearing between the distinct tri-lobe populations. At -30 V/cm (green), the electron mean free path is just a fraction of the crystal dimensions, so most of the propagating charges scatter multiple times on their way to the electrodes, resulting in the corresponding charge density patterns appearing toward the middle of the detector face. At even stronger negative bias fields, the detected charge density patterns remain roughly Gaussian in shape, but with decreasing width for greater field strength and thus decreased electron mean free path.

The evolution of the hole pattern is more straightforward, as the holes propagate along the electric field even at low field strengths, producing a distorted Gaussian shape that shrinks with increasing voltage, as shown in Fig. 3 (right).

Because we observed the relatively small widths of the charge density patterns at the higher field strengths and because widths

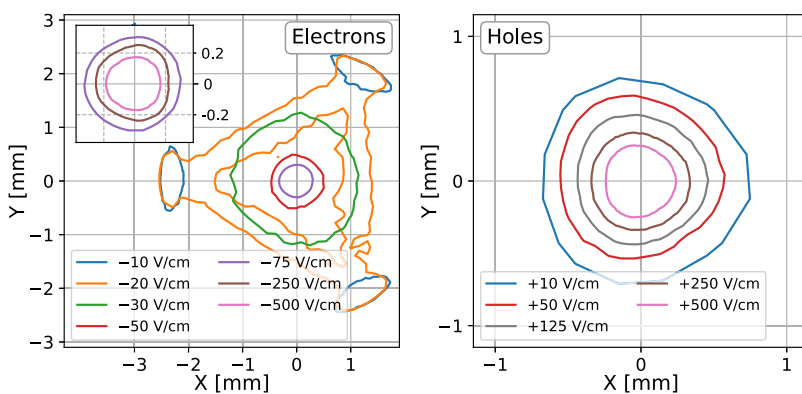


FIG. 3. The 50% contours for the charge density patterns for electrons (left) and holes (right) for electric field strengths up to 500 V/cm . Note the differences of scale between the figures. The electron patterns are much larger at low voltages due to the low rates of intervalley scattering. At high field strengths, they scatter frequently and travel along the average valley direction.

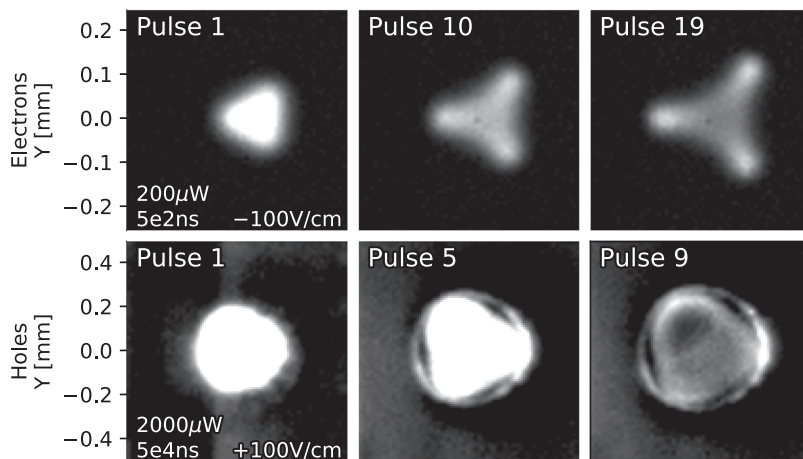


FIG. 4. The evolution of the charge pattern as a function of pulse number for electrons (top row) and holes (bottom row). The white text in the bottom of the first figure in each row shows the power and width of the laser pulse and the bias applied to the crystal.

were also smaller when we decreased the laser power, we suspected that widths were increased by mutual repulsion of drifting charges or by surface charge buildup. Hence, we investigated the electron and hole dynamics more closely.

As mentioned previously, at each point in the raster scan, a train of 20 charge pulses is sent through the crystal. In our initial studies, the resultant voltage pulses were averaged to obtain a single value at each point in the scan. This methodology assumed that the crystal reverts to equilibrium during the 1 ms between consecutive pulses. The basis for this assumption was that the transit time for the charges is on the order of hundreds of nanoseconds,¹² and the recovery time of our amplifier circuit is on the order of 100 μ s.

To test this assumption, we increased the power and duration of the laser pulses. We observed that even at high field strengths of 100 V/cm, the patterns deviated significantly from the Gaussian spot obtained with lower laser intensities. Furthermore, we observed the charge pattern change over the course of the sequence of 20 pulses.

The top row of Fig. 4 shows the evolution of the observed charge density pattern for electrons produced by 200 μ W, 500 ns wide laser pulses in a -100 V cm^{-1} applied electric field. Electrons generated by the first laser pulse in each pulse series produced a fuzzy triangular-shaped pattern at the crystal surface (top-left panel). The pattern was different from the Gaussian-like spot seen at lower intensity [compare to Fig. 3 (left), purple or brown]. Pulses later in the series yielded increasingly distinct triangular patterns. Notably, these triangular shapes [Fig. 4 (top-right)] had the same orientation as the patterns observed previously at a low electric field [Fig. 3 (left), blue or orange], where intervalley scattering was infrequent.

The bottom row of Fig. 4 shows the evolution in the hole pattern as a function of pulse number. In contrast with the electron pattern, the hole collection pattern does not retain the same symmetry as the pulse number is increased; instead, we see that a distinct ring appears outside the fuzzy triangular spot.

Our best explanation for this behavior is that some of the charges from each pulse are not collected by the electrodes and instead get stuck inside the crystal near the back (non-illuminated)

face. The first few charges of the first pulse are unaffected, but later charges from the first pulse and charges from later pulses experience a distorted electric field from the stuck charges as they approach the electrodes. Figure 5 shows the electrostatic solution to a 2D model of the proposed mechanism. Charges drifting upward along $X = 0$ experience a saddle point in the electric field before reaching the surface. Some of these charges then drift horizontally until they reach an area of the surface with low charge density. This results in a charge pattern for the pulse that is more diffuse, with lower charge density at the center compared to the edges.

The model also indicates that this horizontal drift occurs in a region with a relatively low field strength. The re-emergence of the tri-lobe structure in the electron pattern is, therefore, a result of the charges experiencing low rates of intervalley scattering during their horizontal drift.

A low-field region inside the crystal would also explain the hole patterns. The band structure for holes has three valleys, two of

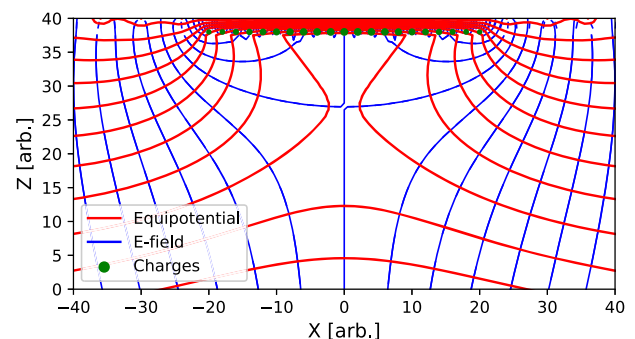


FIG. 5. A 2D toy model of the equipotential and field lines resulting from a series of charges stuck near one face of a parallel plate capacitor. $Z = 40$ represents the back face of the crystal, with the charges placed at $Z = 38$ stretching from $X = -20$ to $X = 20$ with a Gaussian weighting. The front face of the crystal is at $Z = -40$ and is not shown. As charges travel upward along $X = 0$, they will experience a potential minimum at $Z = 27$ and move outward, producing a charge pattern that is brighter near edges than in its center.

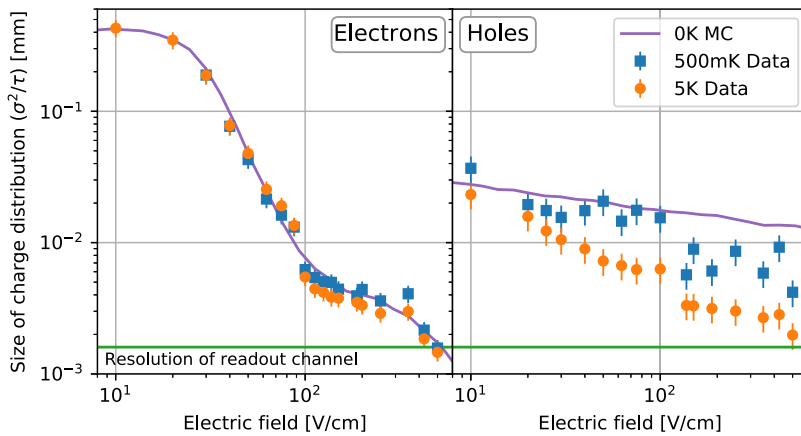


FIG. 6. The relative size of the charge pattern for electrons (left) and holes (right) as measured by the variance of the charge pattern (σ^2) normalized by the crystal thickness (τ). The Monte Carlo (solid line) was fit to the electron data with a physical model involving three free parameters (see text). The Monte Carlo for the holes uses just one free parameter to model their scattering rate.

which are degenerate at zero crystal momentum but anisotropic in position space. The third energy valley for holes (the “split-off” band) is ~ 44 meV higher in energy at zero momentum, but isotropic.^{8,14,19} It appears that the holes are concentrating in this low-field region and filling the lowest energy valleys, forcing some charges into the split-off band. Then, the same horizontal drift phenomenon that occurs with the electrons occurs with the holes. The charges in the lower energy bands drift outward in xy in an anisotropic way, forming a fuzzy triangle, while the charges in the split-off band drift outward isotropically, forming a distinct ring. We believe that this to be the first direct imaging of the split-off band.

To reduce the image distortion from charge trapping for the remainder of the study, we used a 20 dB fiber attenuator to significantly decrease the laser intensity. We then plotted the standard deviation (σ) of the charge pattern size as a function of pulse number (1–20). Noting that the results for the initial pulses for each sequence indicated a σ that increased linearly with pulse number, we fit the σ for the first five pulses with a linear function and used the intercept for this fit in the final result.

The final results of the study are shown in Fig. 6. In this plot, the size of the charge collection pattern, as measured by the variance (σ^2), is normalized by the crystal thickness (τ) to provide a crystal-independent value for the lateral charge diffusion. For the low voltage electron data (< 30 V cm⁻¹), where the tri-lobe pattern is still present, σ^2 is a measurement of the variance of the distribution after being projected onto the x -axis. For the higher voltage electron data, and for the hole data, where the charge pattern is approximately Gaussian, σ^2 was obtained from the Gaussian fit of a 1D scan through the center of the pattern.

Overlaid on each plot are the results of our Geant4 Condensed Matter Physics (G4CMP) simulation software, which we developed to extend the capabilities of Geant4 into the regime of low-temperature charge and phonon transport.²⁰ It includes the electron valleys in silicon and the intervalley scattering process. The scattering is implemented as a Poisson process with a rate function defined by

$$R = \Gamma_I + \Gamma_{ph}|E|^\alpha, \quad (1)$$

where Γ_I and Γ_{ph} are the rate constants associated with impurity scatters, which dominate at low voltage, and phonon-assisted transitions, which dominate at high voltage, respectively. A third constant, α , is used to set the dependence of the phonon-assisted transitions on the electric field (E).

The best-fit parameters for the data up to 500 V cm⁻¹ are $\Gamma_I = 1.5(5) \times 10^6$ Hz, $\Gamma_{ph} = 1.5(3)$ Hz(V/cm)^{- α} , and $\alpha = 4.0(1)$. These values (Γ_{ph} , in particular) differ from the results of our previous paper because the value for the phonon-assisted transition rate was not well constrained for the voltage range we were probing (2–50 V cm⁻¹).

This work was supported, in part, by the U.S. Department of Energy and by the National Science Foundation. This document was prepared by using resources of the Fermi National Accelerator Laboratory (Fermilab), a U.S. Department of Energy, Office of Science, HEP User Facility. Fermilab is managed by Fermi Research Alliance, LLC (FRA), acting under Contract No. DE-AC02-07CH11359. SLAC is operated under Contract No. DEAC02-76SF00515 with the U.S. Department of Energy.

REFERENCES

- R. K. Romani, P. L. Brink, B. Cabrera, M. Cherry, T. Howarth, N. Kurinsky, R. A. Moffatt, R. Partridge, F. Ponce, M. Pyle, A. Tomada, S. Yellin, J. J. Yen, and B. A. Young, *Appl. Phys. Lett.* **112**, 043501 (2018); [arXiv:1710.09335](https://arxiv.org/abs/1710.09335)[physics.ins-det].
- R. Agnese *et al.*, *Phys. Rev. Lett.* **121**, 051301 (2018).
- Z. Hong, R. Ren, N. Kurinsky, E. Figueroa-Feliciano, L. Wills, S. Ganjam, R. Mahapatra, N. Mirabolfathi, B. Nebolsky, H. D. Pinckney, and M. Platt, [arXiv:1903.06517](https://arxiv.org/abs/1903.06517)[physics.ins-det] (2019).
- J. Tiffenberg, M. Sofo-Haro, A. Drlica-Wagner, R. Essig, Y. Guardincerri, S. Holland, T. Volansky, and T.-T. Yu, *Phys. Rev. Lett.* **119**, 131802 (2017); [arXiv:1706.00028](https://arxiv.org/abs/1706.00028)[physics.ins-det].
- SENSEI Collaboration, “SENSEI: Direct-detection constraints on sub-GeV dark matter from a shallow underground run using a prototype skipper CCD,” *Phys. Rev. Lett.* **122**(16), 161801 (2019).
- B. S. Neganov and V. N. Trofimov, *Otkryt. Izobret.* **146**, 215 (1985).
- P. N. Luke, J. Beeman, F. S. Goulding, S. E. Labov, and E. H. Silver, *Nucl. Instrum. Methods Phys. Res., Sect. A* **289**, 406 (1990).

- ⁸R. A. Moffatt, N. A. Kurinsky, C. Stanford, J. Allen, P. L. Brink, B. Cabrera, M. Cherry, F. Insulla, F. Ponce, K. Sundqvist, S. Yellin, J. J. Yen, and B. A. Young, *Appl. Phys. Lett.* **114**, 032104 (2019); [arXiv:1807.07986](https://arxiv.org/abs/1807.07986)[cond-mat.mtrl-sci].
- ⁹C. Jacoboni and L. Reggiani, *Rev. Mod. Phys.* **55**, 645 (1983).
- ¹⁰B. Ridley, *Quantum Processes in Semiconductors* (Oxford Science Publications (OUP), Oxford, 1999).
- ¹¹K. M. Sundqvist, “Carrier transport and related effects in detectors of the cryogenic dark matter search,” Ph.D. thesis, University of California, Berkeley, 2012.
- ¹²C. Canali, C. Jacoboni, F. Nava, G. Ottaviani, and A. Alberigi-Quaranta, *Phys. Rev. B* **12**, 2265 (1975).
- ¹³G. Dresselhaus, A. F. Kip, and C. Kittel, *Phys. Rev.* **98**, 368 (1955).
- ¹⁴E. O. Kane, *J. Phys. Chem. Solids* **1**, 82 (1956).
- ¹⁵M. Cardona and F. H. Pollak, *Phys. Rev.* **142**, 530 (1966).
- ¹⁶Electrodes composed of tri-layer consisting of 40 nm of W on 20 nm of Al and on 40 nm of amorphous Si.
- ¹⁷R. Moffatt, “Two-dimensional spatial imaging of charge transport in Germanium crystals at cryogenic temperatures,” Ph.D. thesis, Stanford University, 2016.
- ¹⁸Mirrorcle Technologies, Inc. <https://www.mirrorcletech.com/products.html>.
- ¹⁹G. Ottaviani, L. Reggiani, C. Canali, F. Nava, and A. Alberigi-Quaranta, *Phys. Rev. B* **12**, 3318 (1975).
- ²⁰D. Brandt, R. Agnese, P. Redl, K. Schneck, M. Asai, M. Kelsey, D. Faiez, E. Bagli, B. Cabrera, R. Partridge, T. Saab, and B. Sadoulet, “Semiconductor phonon and charge transport Monte Carlo simulation using Geant4,” [arXiv:1403.4984](https://arxiv.org/abs/1403.4984)[physics.ins-det] (2014).